Supporting Information

Comparative study of the self-assembly behaviour of 3-chloro-4-hydroxy-phenylazo dyes

Wenke Müller[*a], Ralf Schweins[a], Bernd Nöcker[b], Hans Egold[c] and Klaus Huber[c]

a.   *Institut Laue-Langevin, DS/LSS, 71 Avenue des Martyrs, 38000 Grenoble, France.*
b.   *KAO Germany GmbH, Pfungstädter Straße 98-100, 64297 Darmstadt, Germany.*
c.   *Universität Paderborn, Warburger Straße 100, 33098 Paderborn, Germany.*

E-mail: we-mue@gmx.net

Experimental

UV/vis spectroscopy. UV/vis spectra were recorded using a V-630 spectrometer from Jasco. Hellma quartz glass cuvettes with optical path lengths ranging from 0.01 cm to 1 cm were used for this purpose. The spectrometer was equipped with a thermostat to guarantee a constant measurement temperature of 25 °C. Samples showing precipitation were filtered prior to measurement (MACHEREY-NAGEL, CHROMAFIL Xtra H-PTFE syringe filters, pore size 0.2 µm).

Light Scattering. Light scattering measurements of solutions containing the dye Yellow were performed on an ALV 5000E compact goniometer system using a HeNe laser at a wavelength of 632.8 nm. Light scattering measurements were performed at 13 angles ranging from 30 ° to 150 °. To determine the absolute scattering intensity in terms of the Rayleigh ratio RR of the sample, the solvent scattering $I_{solvent}$ was subtracted from the scattering intensity of the sample I_{sample} and the resulting signal normalized to the scattering intensity $I_{toluene}$ arising from toluene with $RR_{toluene}$ being the Rayleigh ratio of toluene at the given angle.

$$RR = \frac{I_{sample} - I_{solvent}}{I_{toluene}} \cdot RR_{toluene} \tag{1}$$

An aqueous $NaHCO_3/Na_2CO_3$ buffer (pH = 10.5, ionic strength $I \approx 0.25$ M) was used as the solvent. Measurements were performed at 25 °C. Cylindrical cuvettes with a 1 cm inner diameter were used. Samples were filtered prior to measurement (MACHEREY-NAGEL, CHROMAFIL Xtra H-PTFE syringe filters, pore size 0.2 µm).

Light scattering measurements of solutions containing the dye Red were performed on an ALV CGS-3 Compact Goniometer System (ALV GmbH, Langen, FRG) using a HeNe laser at a wavelength of 632.8 nm. Light scattering measurements and data treatment were performed analogous to the above-mentioned procedure. For the creation of a Zimm plot, the contrast factor K was calculated according to:[1]

$$K = \frac{4 \cdot \pi^2}{\lambda_0^4 \cdot N_A} \cdot n_m^2 \cdot \left(\frac{dn}{dc_m}\right)^2 \tag{2}$$

Where $\lambda_0 = 632.8$ nm is the laser wavelength, N_A Avogadro's number, n_m the refractive index of the solvent and $\left(\frac{dn}{dc_m}\right)$ the refractive index increment. The refractive index increment of solutions of Red in an aqueous $NaHCO_3/Na_2CO_3$ buffer with pH = 10.5 and $I \approx 0.25$ M was determined using a differential refractometer (Typ DR-3 from SLS Systemtechnik, Denzlingen, Germany) which is equipped with a diode laser (wavelength: 635 nm).

Small-angle neutron scattering. Samples for small-angle neutron scattering (SANS) measurements were obtained by dissolving the dye Red in a $NaHCO_3/Na_2CO_3$ buffer in D_2O (pD = 10.7, ionic strength $I \approx 0.25$ M). The solution was subsequently filtered (MACHEREY-NAGEL, CHROMAFIL Xtra H-PTFE syringe filters, pore size 0.2 µm) into a dust-free sample vial and equilibrated for a minimum of 20 h at room temperature.

SANS was performed at the small-angle neutron scattering instrument D11 at the Institut Laue-Langevin (Grenoble, France). Different setups were used: (2) The sample containing $[Red]_{tot} = 10$ mM was measured at three sample-to-detector distances (38.0 m collimation 40.5 m), (10.5 m collimation 10.5 m), (1.7 m collimation 2.5 m) at a neutron wavelength of 6 Å to cover a q-range of 0.0014 Å^{-1} to 0.5 Å^{-1}. A circular neutron beam with a diameter of 14 mm was used. (3) The sample containing $[Red]_{tot} \approx 5$ mM was measured at three sample-to-detector distances (38.0 m collimation 40.5 m), (10.5 m collimation 10.5 m), (2.5 m collimation 2.5 m) at a neutron wavelength of 6 Å to cover a q-range of 0.0014 Å^{-1} to 0.5 Å^{-1}. A circular neutron beam with a diameter of 14 mm was used.

Neutrons were detected with a ^{3}He-detector (Reuter-Stokes multi-tube detector consisting of 256 tubes with a tube diameter of 8 mm and a pixel size of 8 mm x 4 mm), detector images azimuthally averaged, corrected to the transmission of the direct beam and scaled to absolute intensity using the Mantid software.[2,3] Solvent scattering and incoherent background were subtracted from the scattering curves.[4] SANS data were collected at a sample temperature of 25 °C.

NMR-spectroscopy. Samples for NMR-spectroscopy were obtained by dissolving the dye Red in a $NaHCO_3/Na_2CO_3$ buffer in D_2O (pD=10.7, ionic strength $I \approx 0.25$ M). The solution was subsequently filtered (MACHEREY-NAGEL, CHROMAFIL Xtra H-PTFE syringe filters, pore size 0.2 µm) into the NMR-tube. 2-dimensional rotating frame nuclear overhauser effect spectroscopy- (EASY ROESY) spectra were recorded with a NMR Ascent 700 spectrometer (700 MHz) equipped with a cryogenic probe with z-gradient at 298 K. The ROESY field strength was 5000 Hz. The magnetization was locked at an angle of 45 ° off the z-axis which ensures suppression of TOCSY artefacts. Chemical shifts were referenced to residual HDO.[5]

Results and discussion

Solubility of three dyes. The solubility of Yellow, Blue and Red in the aqueous $NaHCO_3/Na_2CO_3$ buffer (pH = 10.5, ionic strength $I \approx 0.25$ M) at 25 °C was studied by means of UV/vis spectroscopy. In the absence of precipitation and at a wavelength where self-aggregation does not have an effect on dye absorption, the molar extinction coefficient does not depend

on dye concentration. Therefore, a plot of sample absorbance divided by path-length (A_d) vs dye concentration $[Dye]_{tot}$ should result in a linear relationship. Figure SI1 shows these plots for all three dyes.
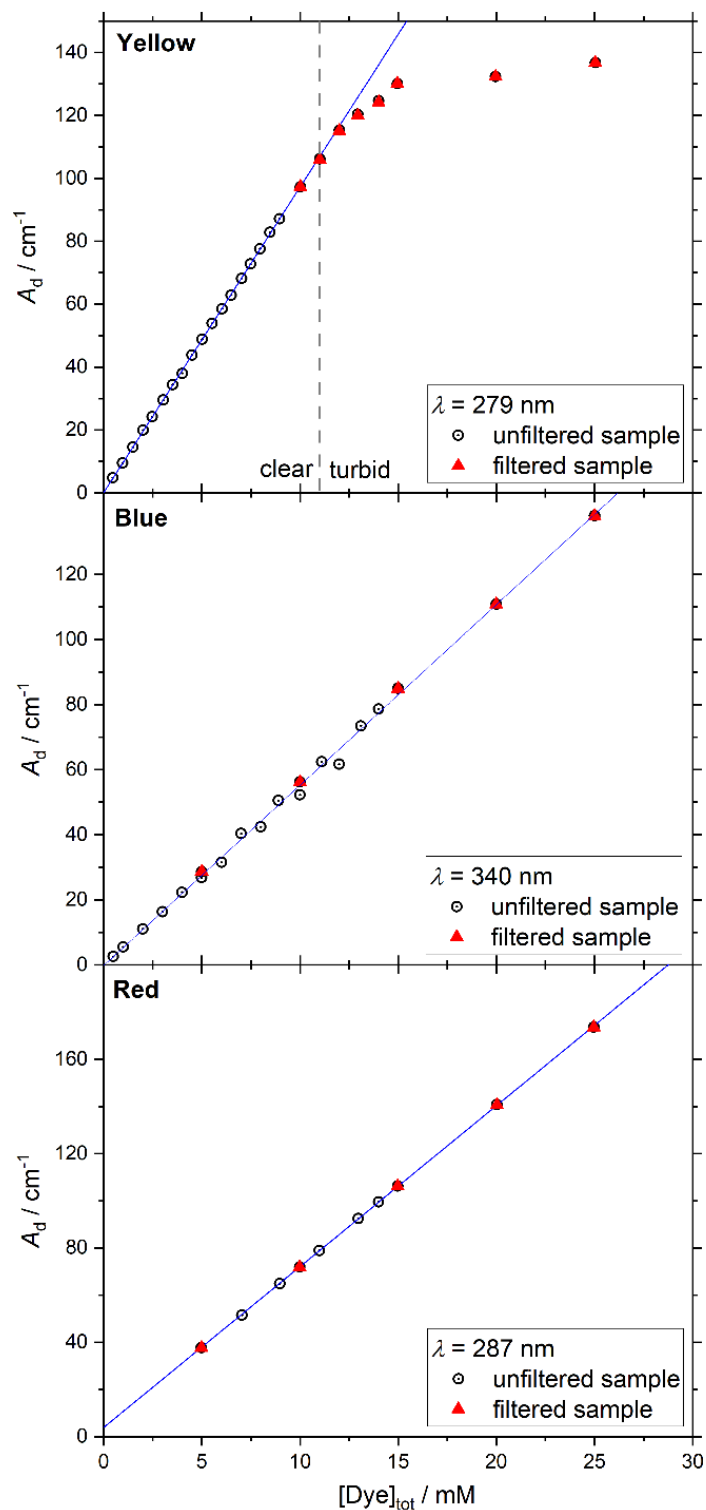
Figure SI1: Solubility of dyes in an aqueous $NaHCO_3/Na_2CO_3$ buffer at 25 °C investigated with UV/vis spectroscopy. Spectra were recorded the day after sample preparation.

Spectra of Yellow do not depend on concentration. For Red and Blue, A_d was evaluated at a wavelength, where dye absorption is not influenced by its self-aggregation. This wavelength corresponds to the position of an absorption maximum at lower wavelengths compared to the main peak. A_d of filtered and unfiltered samples were compared. Filtration was done

3

on a sample basis and for samples visually showing phase separation. Filters with a pore size of 0.2 μm were used (MACHEREY-NAGEL, CHROMAFIL Xtra H-PTFE syringe filters). Within the observed concentration range, only the dye Yellow shows a solubility limit at $[Yellow]_{tot} = 11$ mM, which is observed visually and by a deviation from Beer-Lambert law. Solutions containing Blue and Red do not show this solubility limit within the observed timeframe, i.e. one day after sample preparation.

Solubility of Yellow. Figure SI2 shows UV/vis absorption spectra of the dye Yellow at various concentrations. Different to Blue and Red, the absorption spectrum of Yellow does not change with concentration. This points towards an absence of concentration-induced aggregation in the $NaHCO_3/Na_2CO_3$-buffer.
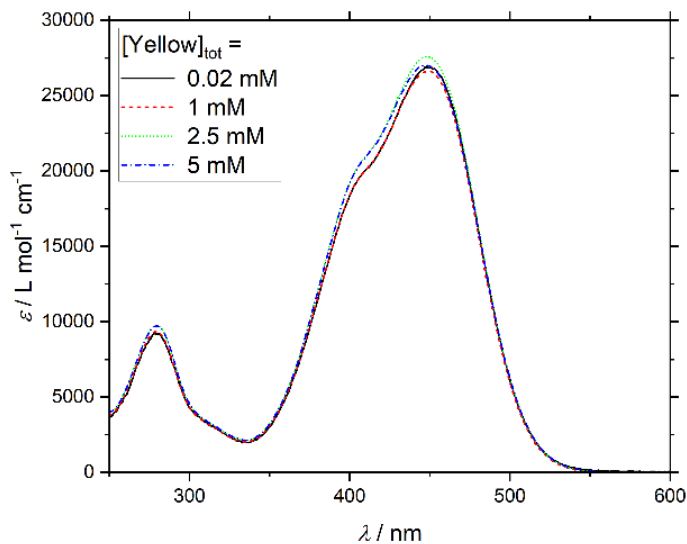
Figure SI2: UV/vis absorption spectra of the dye Yellow recorded at four different concentrations in an aqueous $NaHCO_3/Na_2CO_3$ buffer at 25 °C.

Absence of self-aggregation of Yellow was confirmed by light scattering. Combined static and dynamic light scattering (SLS and DLS) was performed on solutions containing between 0.5 mM and 10 mM of Yellow. First of all, RR detected by SLS did not depend on the scattering angle. Therefore, RR obtained at different measurement angles were averaged to yield RR_{avg} and plotted against the concentration of Yellow in the corresponding sample. The resulting linear relationship between RR_{avg} and $[Yellow]_{tot}$ is shown in Figure SI3 and confirms the absence of concentration-induced aggregation. The absence of a correlation function in DLS-measurements (Figure SI4) confirms the absence of aggregates.
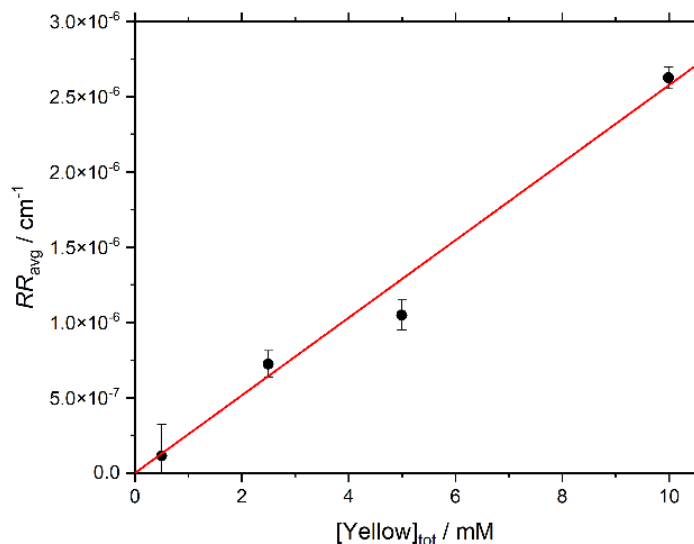
Figure SI3: Rayleigh ratio of samples containing Yellow at various concentrations in the $NaHCO_3/Na_2CO_3$ buffer at 25 °C. The Rayleigh ratio was obtained by SLS and averaged over all angles due to the absence of an angular dependency. The red line displays a linear fit to the data.

4
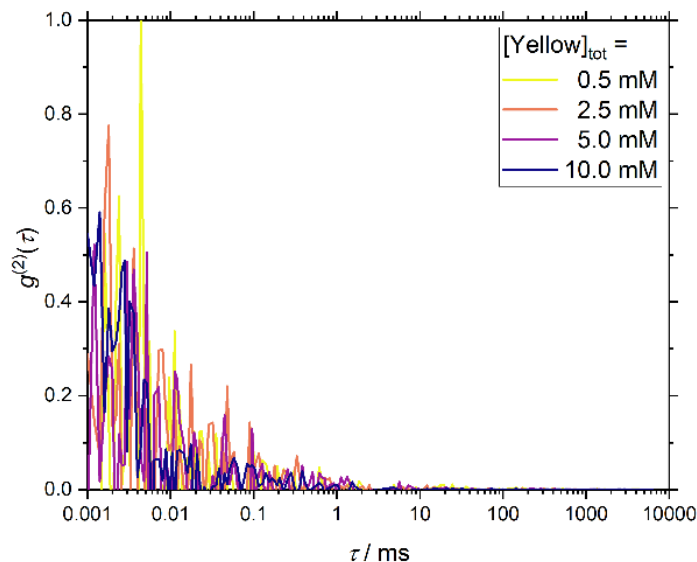
Figure SI4: DLS intensity correlation functions $g^{(2)}(\tau)$ of samples containing varying concentrations of Yellow in the Na-HCO$_3$/Na$_2$CO$_3$ buffer at 25 °C.

Application of exciton theory to determine Blue dimer geometry. The dimer spectrum of Blue shows two clearly discernible peaks with absorption maxima at energies higher and lower than that of the monomer. This can be explained by exciton theory:[6] Upon dimerization, the first excited energy state of the monomer splits into two due to dipole-dipole interaction between the two interacting molecules.[6–9] For quantitative calculations, the ground state of the monomer is assumed to remain unaffected during dimerization.[8] The dimer splitting depends on transition dipole moments and on dimer geometry.[9] As the planar character of the mostly aromatic molecule Blue suggests π-stacking as one of the preferred types of intermolecular interactions, two possible dimer geometries depicted in Figure SI5 were further investigated: The model of coplanar inclined transition dipoles (Figure SI5(A)) and the model of non-planar transition dipoles (Figure SI5(B)).[10]
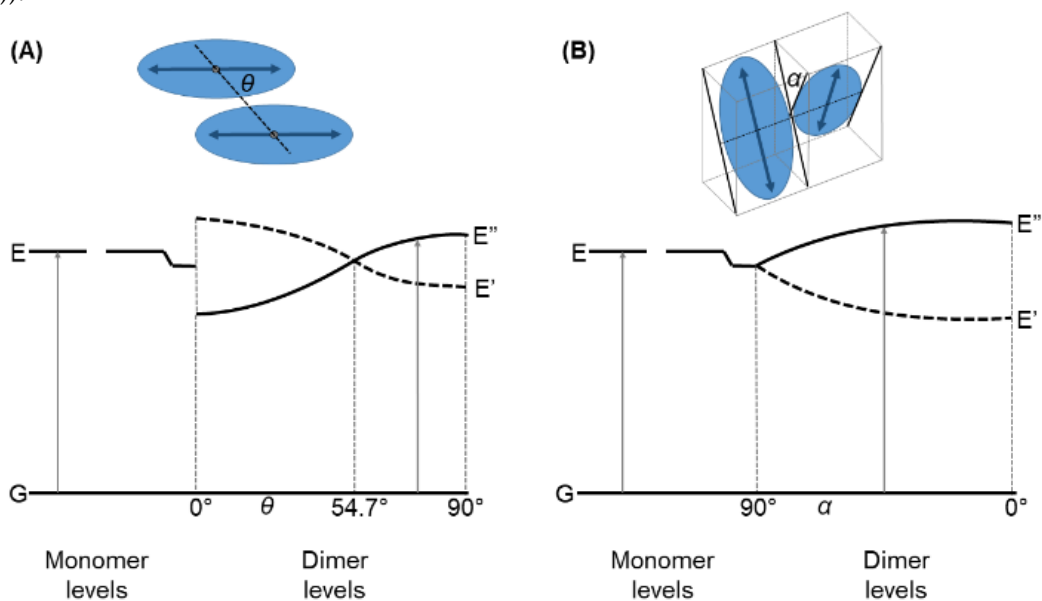
Figure SI5: (A) Schematic and exciton band energy diagram for a molecular dimer with coplanar transition dipoles. (B) Schematic and exciton band energy diagram for a molecular dimer with non-planar transition dipoles and an angle α between molecular planes. The schemes were adopted from Kasha et al.[10]

Both geometries are simple and permit simultaneous H-band and J-band absorption with the blue-shifted H-band showing a larger intensity than the red-shifted J-band.[8] The asymmetry of functional groups in the molecule Blue may lead to deviations from a precisely coplanar arrangement of transition dipole moments. Nevertheless, both geometries are assumed to be reasonable enough to calculate structural features of the dimer.

5

Within the model of coplanar inclined transition dipoles (Figure SI5(A)) the angle θ made by the polarization axes of the unit molecule with the line of molecular centers and the interplanar spacing R can be calculated according to:[8,10]

$$\theta = \arctan\left(\frac{f_H^2}{f_J^2}\right) \tag{3}$$

$$R = \left(\frac{2.14 \cdot 10^{10} \cdot f_M \cdot (1 - 3\cos^2\theta)}{\tilde{\nu}_M \cdot \Delta\tilde{\nu}_{H,J}}\right)^{\frac{1}{3}} \quad \text{in [Å]} \tag{4}$$

f_J, f_H and f_M are the oscillator strengths of the J-band, the H-band and the monomer respectively. $\tilde{\nu}_M$ is the absorbance maximum position of the monomer in [cm^{-1}] and $\Delta\tilde{\nu}_{H,J} = \tilde{\nu}_H - \tilde{\nu}_J$ the dimer splitting in [cm^{-1}].

Assuming the model of non-planar transition dipoles (Figure SI5(B)), the angle θ is considered to be zero and an angle α describes the torsion between two molecular planes. This difference in geometry also needs to be considered when calculating the interplanar spacing R:[8,11,12]

$$\alpha = 2 \cdot \arctan\sqrt{\frac{f_J}{f_H}} \tag{5}$$

$$R = \left(\frac{2.14 \cdot 10^{10} \cdot f_M \cdot \cos\alpha}{\tilde{\nu}_M \cdot \Delta\tilde{\nu}_{H,J}}\right)^{\frac{1}{3}} \quad \text{in [Å]} \tag{6}$$

The oscillator strength f of any transition can be calculated from the area under the respective band according to:[13]

$$f = 4.32 \cdot 10^{-9} \frac{\text{mol cm}^2}{\text{L}} \int_{\text{band}} \epsilon \, d\tilde{\nu} \tag{7}$$

Where ϵ is the molar extinction coefficient in [L mol^{-1} cm^{-1}] and $\tilde{\nu}$ the wavenumber in [cm^{-1}].

To obtain oscillator strengths f and absorption maximum positions of relevant transitions, monomer- and dimer-spectrum were described with Gauss-functions. This can be justified by various spectral line broadening effects such as interaction between absorbing species and solvent, Doppler broadening and limitations on resolution.[14]

The monomer spectrum exhibits a weak vibrational fine structure. To obtain the fundamental mode of vibronic transitions $\Delta\tilde{\nu}_{\text{vib}}$, the fourth derivative of the spectrum was calculated to make possible a more precise localization of transitions contributing to the monomer spectrum (Figure SI6).[12]
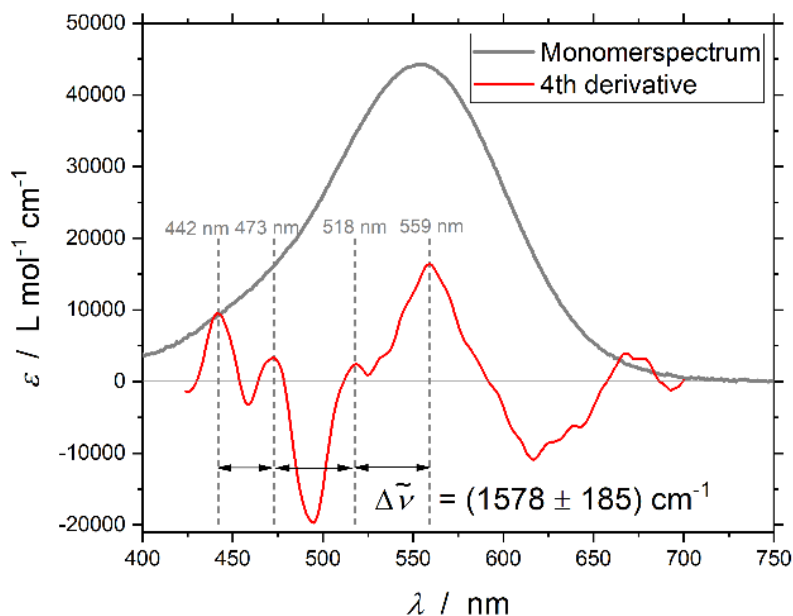
Figure SI6: Monomerspectrum of Blue recorded at [Blue]$_{\text{tot}}$ = 5 µM (grey line) and its 4$^{\text{th}}$ derivative (red line).

Four components with their maxima being separated by $\Delta\tilde{\nu}_{\text{vib}} = (1578 \pm 185)$ cm^{-1} were resolved. This likely corresponds to the fundamental mode of a single vibronic progression according to:

$$\tilde{\nu}_{M,i} = \tilde{\nu}_M + i \cdot \Delta\tilde{\nu}_{\text{vib}} \quad i = 1, 2, 3, \dots \tag{8}$$

The value $\Delta\tilde{\nu}_{\mathrm{vib}}$ determined for the fundamental mode is reasonable, as fundamental modes of aromatic compounds typically lie around 1400 cm^{-1}.[15] Following this analysis, the monomer spectrum was best described with one vibrational progression, taking into account four bands with Gaussian line shape and fixed positions as obtained by derivative analysis in Figure SI6. Therefore, the molar extinction coefficient of the monomer $\epsilon_{\mathrm{M}}(\tilde{\nu})$ as a function of wavenumber $\tilde{\nu}$ was described by the following equation:

$$\epsilon_{\mathrm{M}}(\tilde{\nu}) = \frac{A_{\mathrm{M}}}{w_{\mathrm{M}} \cdot \sqrt{\frac{\pi}{2}}} \exp\left[\frac{-2 \cdot (\tilde{\nu} - \tilde{\nu}_{\mathrm{M}})^2}{w_{\mathrm{M}}^2}\right] + \sum_{i=1}^{3} \frac{A_{\mathrm{M},i}}{w_{\mathrm{M},i} \cdot \sqrt{\frac{\pi}{2}}} \exp\left[\frac{-2 \cdot (\tilde{\nu} - \tilde{\nu}_{\mathrm{M},i})^2}{w_{\mathrm{M},i}^2}\right] \tag{9}$$

A_{M} and $A_{\mathrm{M},i}$ correspond to the area under the respective Gauss function and therefore directly replace the integral in equation (7). w_{M} and $w_{\mathrm{M},i}$ describe peak width and correspond to double the standard deviation from the peak maximum. $\tilde{\nu}_{\mathrm{M}}$ and $\tilde{\nu}_{\mathrm{M},i}$ denote peak positions and were kept constant following equation (8). Fitted Gaussian bands are shown in Figure SI7(A) and the calculated oscillator strength f_{M} is given in Table SI1.

A similar analysis was carried out to describe the dimer spectrum with Gauss functions, taking into account the J-band and the H-band. As the dimer spectrum does not show a distinct vibrational fine structure, the same fundamental vibrational mode $\Delta\tilde{\nu}_{\mathrm{vib}} = (1578 \pm 185)$ cm^{-1} as for the monomer spectrum was assumed for the vibronic progression of the H-band. Due to its comparably small intensity, a vibronic progression of the J-band was not considered.[12] Therefore, keeping peak positions constant, the dimer spectrum was best described with six Gaussian bands: $\tilde{\nu}_{\mathrm{J}} = 15868$ cm^{-1}, $\tilde{\nu}_{\mathrm{H}} = 17889$ cm^{-1} and:

$$\tilde{\nu}_{\mathrm{H},i} = \tilde{\nu}_{\mathrm{H}} + i \cdot \Delta\tilde{\nu}_{\mathrm{vib}} \quad i = 1, 2, 3, \ldots \tag{10}$$

$$\epsilon_{\mathrm{D}}(\tilde{\nu}) = \frac{A_{\mathrm{J}}}{w_{\mathrm{J}} \cdot \sqrt{\frac{\pi}{2}}} \exp\left[\frac{-2 \cdot (\tilde{\nu} - \tilde{\nu}_{\mathrm{J}})^2}{w_{\mathrm{J}}^2}\right] + \frac{A_{\mathrm{H}}}{w_{\mathrm{H}} \cdot \sqrt{\frac{\pi}{2}}} \exp\left[\frac{-2 \cdot (\tilde{\nu} - \tilde{\nu}_{\mathrm{H}})^2}{w_{\mathrm{H}}^2}\right] + \sum_{i=1}^{4} \frac{A_{\mathrm{H},i}}{w_{\mathrm{H},i} \cdot \sqrt{\frac{\pi}{2}}} \exp\left[\frac{-2 \cdot (\tilde{\nu} - \tilde{\nu}_{\mathrm{H},i})^2}{w_{\mathrm{H},i}^2}\right] \tag{11}$$

The result is visualized in Figure SI7(B). Inserting A_{J} and A_{H} as the integral in equation (7), oscillator strengths f_{J} and f_{H} of the respective bands were obtained (Table SI1).

Applying equations (3) and (4) for the calculation of parameters describing the dimer geometry of coplanar inclined transition dipoles leads to an inclination angle $\theta = 89°$. This is very close to $\theta = 90°$, i.e. the absence of inclination, and confirms the presence of H-aggregated dimers. In addition to that it strengthens an analysis according to the dimer geometry of non-planar transition dipoles without inclination. Within this model, a tilt angle $\alpha = 42°$ and an interplanar spacing $R = 5.2$ Å was obtained, which is comparable to $R = 5.7$ Å obtained within the previous model. These values are reasonable. In literature, values between 3.4 Å and 8.3 Å were reported for the interplanar spacing between dye molecules containing aromatic units.[11,12,16]

Table SI1: Peak positions and oscillator strengths of transitions into the vibrational ground state of excited electronic state(s) for the monomer and the dimer of Blue. Results from analysis according to exciton theory are shown.

Monomerspectrum	
$\tilde{\nu}_{\mathrm{M}}$ [cm^{-1}]	17 889
Fundamental mode $\Delta\tilde{\nu}_{\mathrm{vib}}$ [cm^{-1}]	1 578 ± 185
f_{M}	0.51
Dimerspectrum	
$\tilde{\nu}_{\mathrm{J}}$ [cm^{-1}]	15 868
f_{J}	0.11
$\tilde{\nu}_{\mathrm{H}}$ [cm^{-1}]	19 125
f_{H}	0.73
Dimer splitting $\Delta\tilde{\nu}_{\mathrm{H,J}}$ [cm^{-1}]	3 257
Exciton Model: Coplanar inclined transition dipoles	
Inclination angle θ [°]	89
Interplanar spacing R [Å]	5.7
Exciton Model: Non-planar transition dipoles	
Tilt angle α [°]	42
Interplanar spacing R [Å]	5.2
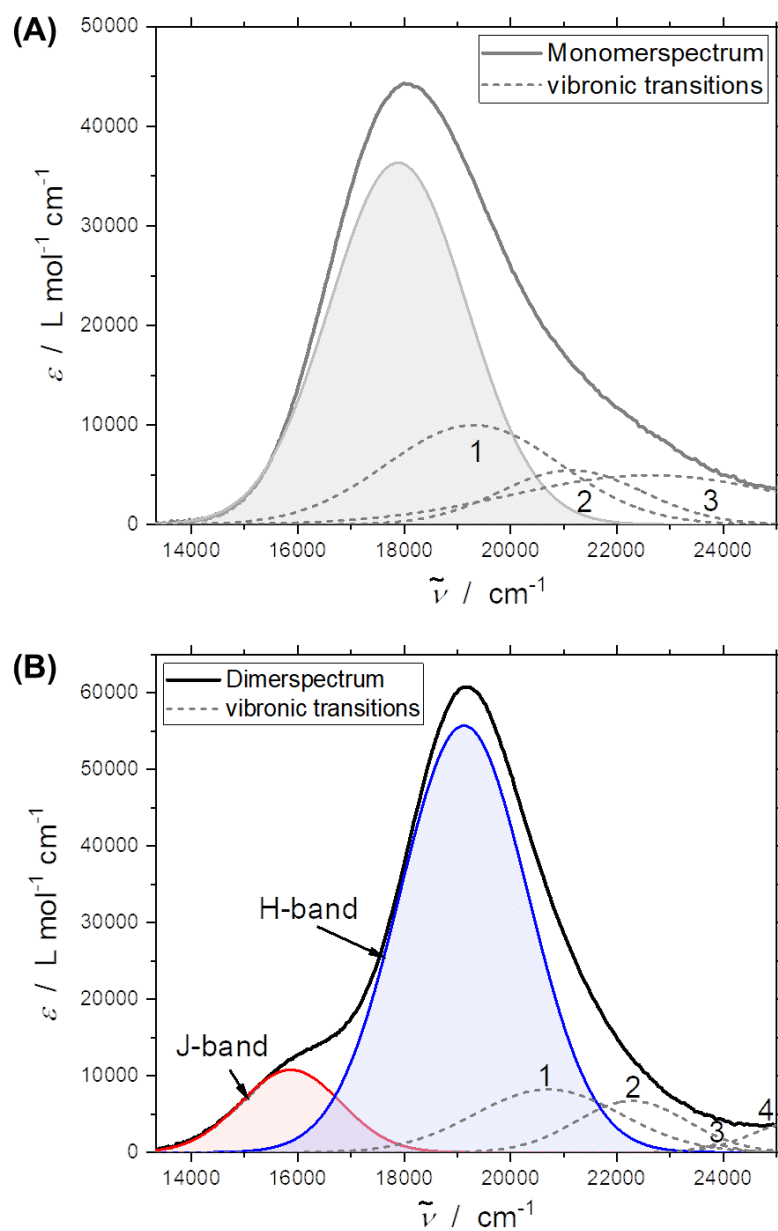
Figure SI7: (A) Monomer spectrum of Blue recorded at $[Blue]_{tot}$ = 5 µM (grey line) and underlying Gaussian bands. (B) Dimer spectrum of Blue (black line) and underlying Gaussian bands.

Guinier analysis of SANS curves of Blue solutions
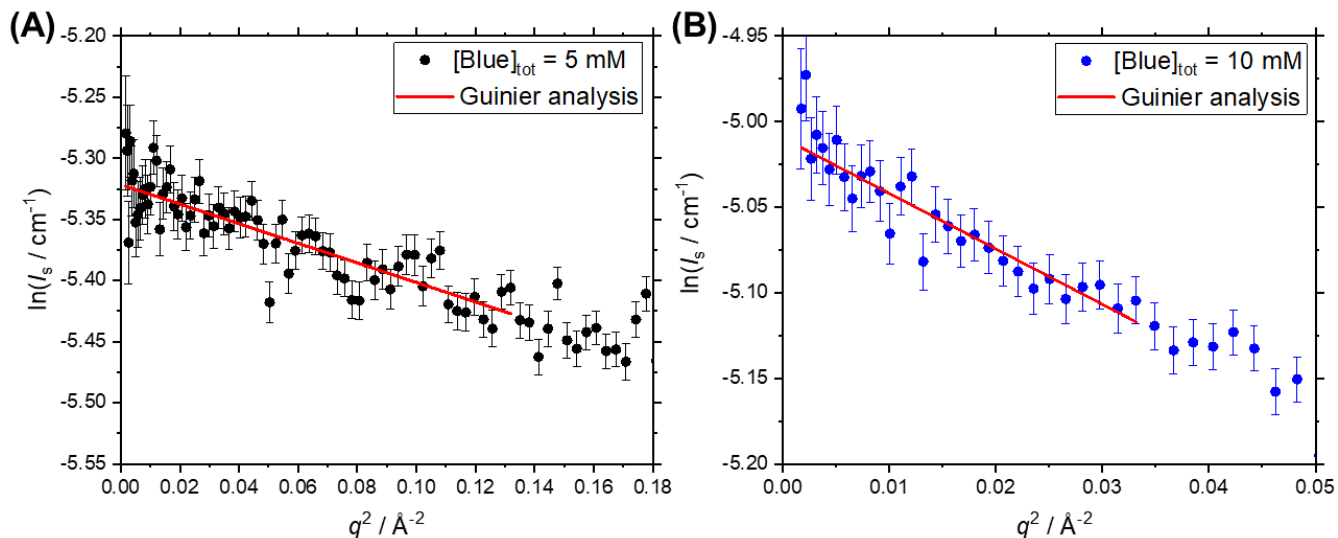
Figure SI8: Guinier analysis of linearized SANS curves of solutions containing (A) $[Blue]_{tot}$ = 5mM and (B) $[Blue]_{tot}$ = 10 mM in an $NaHCO_3/Na_2CO_3$ buffer with pD = 10.7 and $I \approx 0.25$ M prepared in D_2O. Results were given in Table 1 in the main text.

Theoretical calculation of radius of gyration of Blue dimer. The radius of gyration R_g of a homogeneous cylinder can be calculated according to the following equation:[17]

$$R_g^2 = \frac{b^2}{2} + \frac{L^2}{12} \tag{12}$$

b is the radius and L the length of the cylinder. Even though a dimer consisting of two Blue molecules is likely not correctly described with a homogeneous cylinder model, it gives a first approximation of its radius of gyration. The cylinder radius was assumed to be half the distance between the negatively charged oxygen ion of the alkoxide group and the carbon atom in position 7 of the aromatic 2,1-benzoisothiazole subunit: $b = 0.5 \cdot 10.5$ Å = 5.25 Å. The cylinder length was assumed to correspond to the interplanar spacing between two transition dipole moments: $L = R = 5.2$ Å determined by exciton theory. This yields $R_g \approx 4$ Å.
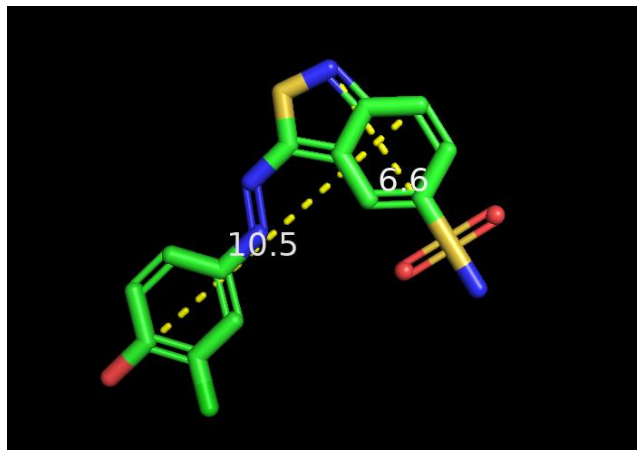
Figure SI9: Chemical structure of dissociated Blue, not including hydrogen atoms, and distances between some atoms generated with the software PyMOL.[18] Distances are given in Å.

Red self-aggregation. SANS curves of two solutions of Red were shown in Figure 8 in the main text. One solution contained $[Red]_{tot}$ = 10 mM and the other one was intended to contain $[Red]_{tot}$ = 15 mM. The latter was filtered too soon after its preparation, resulting in a loss of Red which was not completely dissolved and therefore a reduction of dye concentration to $[Red]_{tot} < 10$ mM. This is visible by a lower incoherent background for this sample compared to the one containing $[Red]_{tot}$ = 10 mM. In order to obtain an idea about the actual dye concentration in this sample, its SANS forward scattering intensity I_o was compared to that of the sample with $[Red]_{tot}$ = 10 mM, I_o being determined by Guinier analysis. The corresponding analysis is shown in Figure SI10 with results given in the caption. As I_o of the sample with unknown Red concentration was determined to be approximately half the forward scattering intensity of the sample with $[Red]_{tot}$ = 10 mM,

its concentration is approximated to be $[Red]_{tot} \approx 5$ mM. Not precisely knowing the concentration of Red does not pose a big problem as no absolute analysis of scattering intensities was performed here. Both SANS curves of solutions of Red displayed in the main text (Figure 8) show similar slopes and features and the radii of gyration obtained by Guinier analysis in the high-q-region are almost identical (Table SI2). Therefore, the same model was applied to fit both SANS curves simultaneously, permitting the incoherent background and volume fractions to differ. Results from form factor fitting with the sum of a fractal form factor and a Guinier fit are given in Table SI2.[19] The fractal describes the mid- and low-q region and is characterized by the radius of spherical building blocks, R_{block}, its scattering length density ρ_{block}, the fractal dimension D_f and the cluster correlation length L_{corr}, which represents the total fractal cluster size. ϕ_{block} is the volume fraction of spherical building blocks. As size parameters were kept constant, fits only differ in scaling of the Guinier and the fractal contribution.
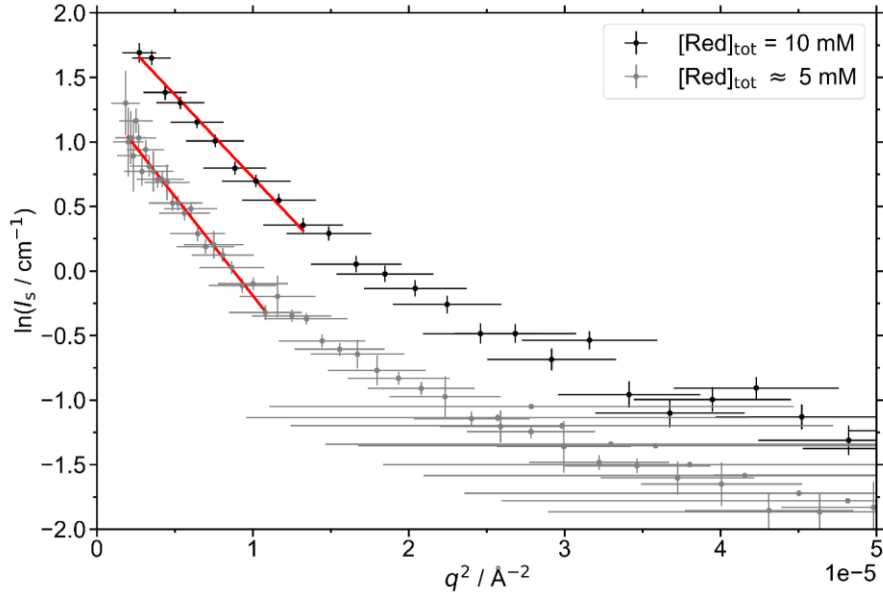
Figure SI10: Guinier analysis and linearized SANS curves of solutions containing Red at a concentration of 10 mM and approximately 5 mM. Solutions were prepared in a $NaHCO_3/Na_2CO_3$ buffer in D_2O with pD = 10.7 and $I \approx 0.25$ M. Results of Guinier analysis for $[Red]_{tot} = 10$ mM: $I_0 = (7.4 \pm 0.3)$ cm^{-1}, $R_g = (620 \pm 13)$ Å, for $[Red]_{tot} \approx 5$ mM: $I_0 = (3.8 \pm 0.2)$ cm^{-1}, $R_g = (679 \pm 13)$ Å.

Table SI2: SANS analysis of two solutions of Red. A form factor consisting of additive contributions from a Guinier-fit and a fractal model was used.[19]

Guinier Analysis, high-q	$[Red]_{tot} = 10$ mM	$[Red]_{tot} \approx 5$ mM
R_g [Å]	8.7 ± 0.2	8.5 ± 0.1
Fit: Guinier + Fractal	$[Red]_{tot} = 10$ mM	$[Red]_{tot} < 10$ mM
$BG_{incoherent}$ [cm^{-1}]	0.001357 (fixed)	0.001015 (fixed)
Scale (Guinier)	0.0019 ± 0.0003	0.00120 ± 0.00007
R_g(Guinier) [Å]	8.5 (fixed)	
Scale (Fractal)	0.009 ± 0.001	0.0043 ± 0.0005
R_{block} [Å]	9 ± 1	
D_f	2.66 ± 0.03	
L_{corr} [Å]	437 ± 10	
ϕ_{block}	0.0022 (fixed)	
ρ_{block} [10^{-6} Å^{-2}]	2.642 (fixed)	
ρ_{solv} [10^{-6} Å^{-2}]	6.376 (fixed)	
χ^2_{red}	1.5175	3.3116

10

An alternative to describing the recorded SANS curves with a fractal form factor could be the sum of a star form factor and the form factor of a smaller species, which would exist in equilibrium and act as a building block for the larger structure. Considering π-π-stacking interactions to be of major relevance to the aggregation of Red, the presence of cylindrical core aggregates is likely. However, the use of only a cylinder model to describe recorded SANS curves is not plausible due to several characteristics of the curve: First of all, a $I_s \propto q^{-2.66}$ slope is observed in the low- to mid-q region. Second of all, the Kratky plot of the curves (Figure SI11(A)) shows an initial maximum before an approximately linear increase of the curve is observed. Third of all, a minimum can be seen in the Holtzer plot (Figure SI12(A)) before a plateau value is reached. The plateau value is characteristic for rod-like aggregates.[20] Both, the maximum in the Kratky plot and the minimum in the Holtzer plot point towards a rather compact structure, which could result from branching and network formation due to overlap of the cylindrical core aggregates.[21,22] A possibility to describe branching points would be the application of a form factor model for stars, which considers the existence of specific star centres.[21,23] Huber et al. performed Monte Carlo calculations to determine such form factors for star-branched polymers. The Kratky- and Holtzer plot of example form factors for polymer stars of different sizes, the size being indicated by the number of bonds n_B, are shown in Figure SI11(B) and Figure SI12(B) respectively.[21] These form factors show similar features in the Kratky- and Holtzer-plot compared to the curves recorded from solutions of Red: Firstly, the initial maximum in the Kratky plot is well present and secondly, a minimum can be observed in the Holtzer plot before a plateau value is reached. Considering branching due to the overlap of cylindrical core aggregates of Red, the sum of a star form factor and the form factor of a cylinder could therefore be a reasonable model to describe the observed SANS curves from Red solutions.
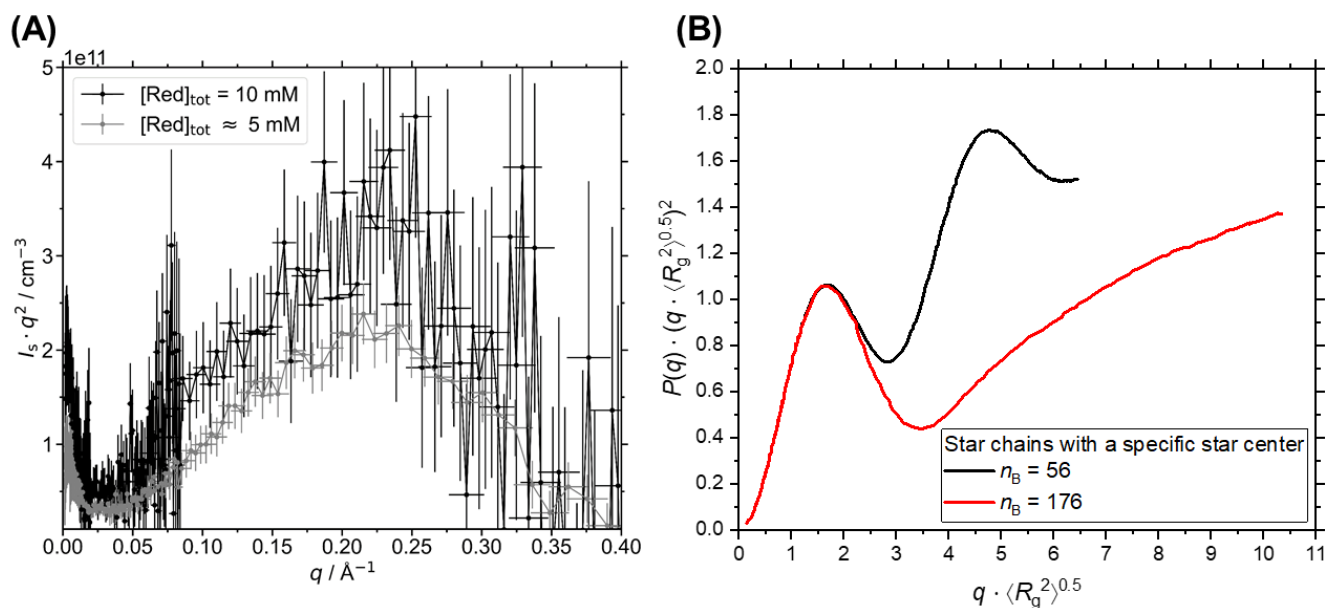
Figure SI11: (A) Kratky plot of SANS curves from solutions containing Red at a concentration of 10 mM and 5 mM. Solutions were prepared in a NaHCO$_3$/Na$_2$CO$_3$ buffer in D$_2$O with pD = 10.7 and $I \approx 0.25$ M. (B) Kratky plot of a form factor model for star polymer chains with a specific star center as calculated by Huber et al.[21] The size of the polymer is indicated by the number of bonds, n_B. R_g is the radius of gyration and $P(q)$ the form factor.
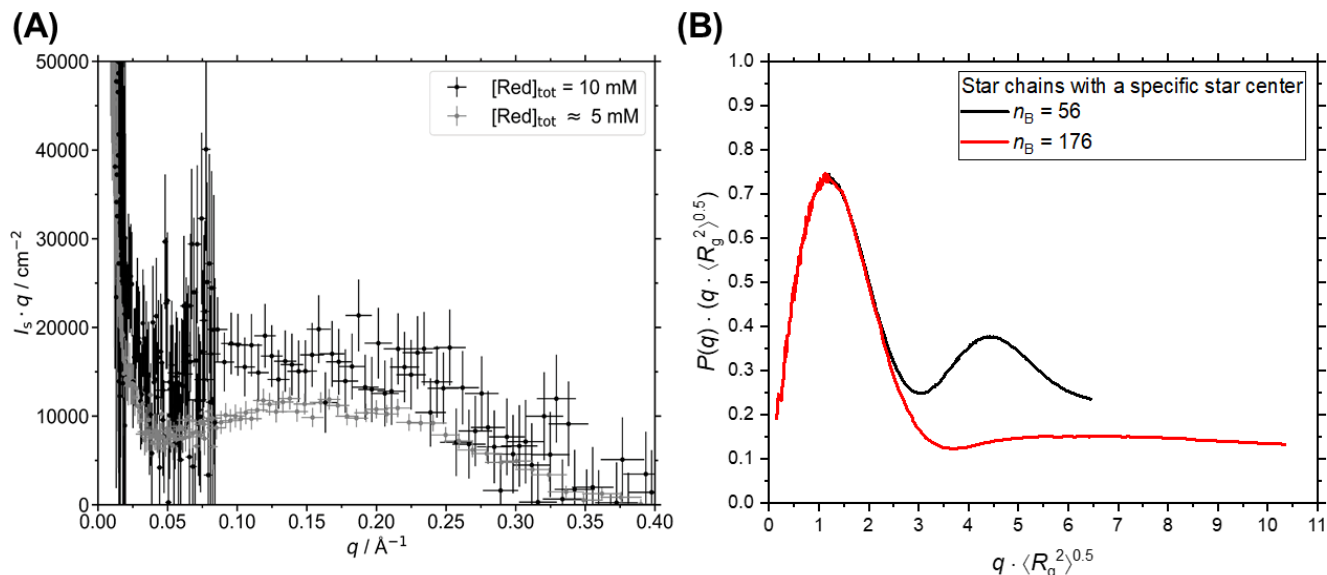
Figure SI12: (A) Holtzer plot of SANS curves from solutions containing Red at a concentration of 10 mM and 5 mM. Solutions were prepared in a NaHCO$_3$/Na$_2$CO$_3$ buffer in D$_2$O with pD = 10.7 and $I \approx 0.25$ M. (B) Holtzer plot of a form factor model for star polymer chains with a specific star center as calculated by Huber et al.[21] The size of the polymer is indicated by the number of bonds, n_B. R_g is the radius of gyration and $P(q)$ the form factor.
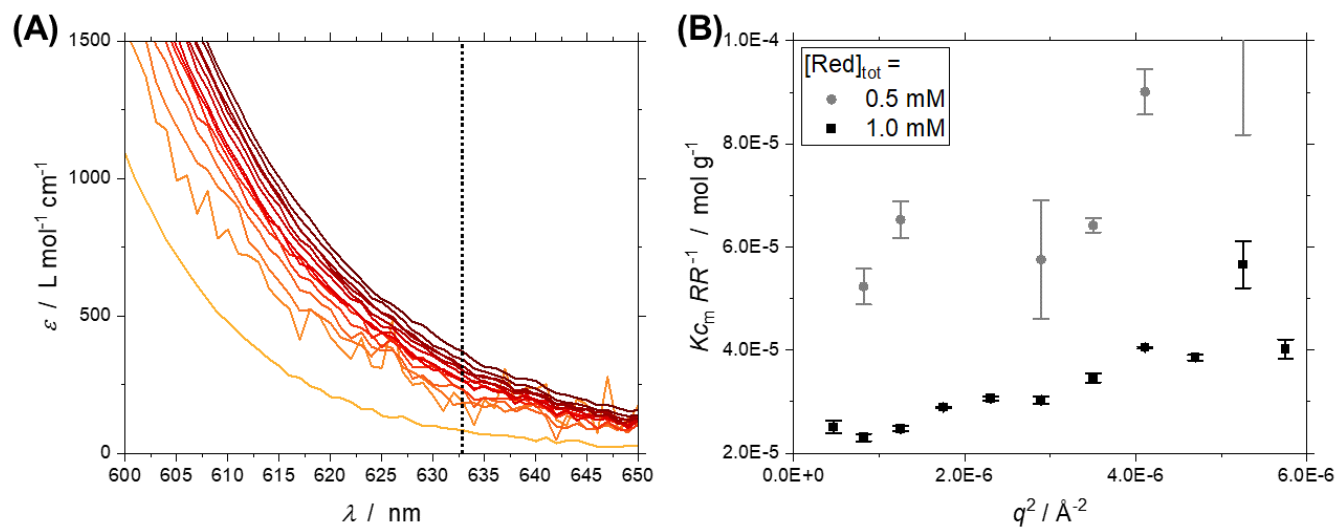
Figure SI13: (A) Section of UV/vis absorption spectra from solutions of Red containing 0.02 mM < [Red]$_{tot}$ < 6 mM (yellow to dark red lines). The wavelength, at which light scattering measurements can be performed is indicated by a vertical, dotted line. (B) Apparent Zimm plot of Rayleigh ratios resulting from static light scattering on solutions containing either [Red]$_{tot}$ = 0.5 mM or [Red]$_{tot}$ = 1.0 mM in an NaHCO$_3$/Na$_2$CO$_3$ buffer with pH = 10.5 and $I \approx 0.25$ M prepared in H$_2$O. Rayleigh ratios were not corrected for absorption. K was calculated based on the following values: λ_0 = 632.8 nm, n_m = 1.3326, $\left(\frac{dn}{dc_m}\right)$ = 0.000339 mL mg^{-1}. c_m is the mass concentration of the solute.

To extend the available q-range and to confirm findings from SANS measurements, it was attempted to perform light scattering measurements on solutions of Red. However, data quality and the available concentration range is strongly reduced by absorption of the dye Red at the wavelength of λ = 632.8 nm available for light scattering measurements (Figure SI13(A)). Therefore, only a short qualitative discussion of light scattering data obtained from solutions containing [Red]$_{tot}$ = 0.5 mM and [Red]$_{tot}$ = 1 mM is given here. A Zimm-plot of static light scattering data is displayed in Figure SI13(B) and shows a strong angular dependency of the scattered intensity, which confirms the existence of rather large assemblies like it was already shown by SANS. Furthermore, the presence of aggregates is confirmed by the existence of a correlation function from dynamic light scattering measurements.

This is shown exemplarily for two angles in Figure SI14. Theoretically, the intensity correlation function $g^{(2)}(\tau)$ should approach a value of 0.33 for low correlation times τ, which is specific to the setup of the light scattering device. However, data quality is hampered by the absorption of the dye Red and it was therefore abstained from quantitative analysis.
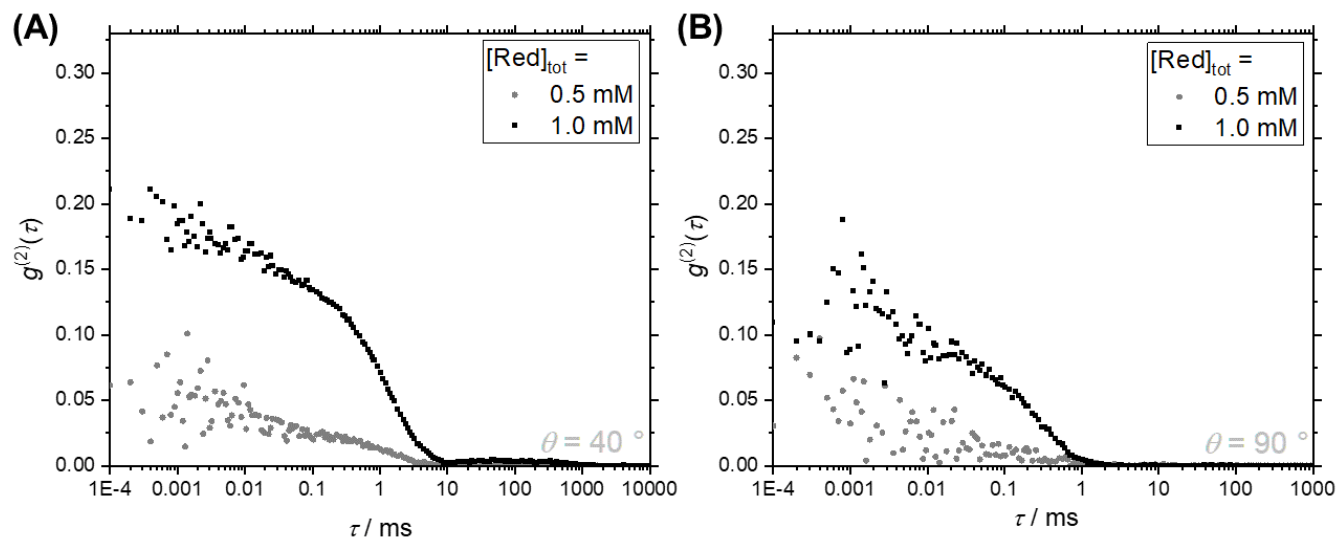
Figure SI14: Intensity correlation functions $g^{(2)}(\tau)$ of solutions of Red in an aqueous $NaHCO_3/Na_2CO_3$ buffer (pH = 10.5, $I \approx 0.25$ M) from dynamic light scattering. (A) Measurement at a scattering angle of 40 °, (B) Measurement at a scattering angle of 90 °.

Figure SI15 shows the ROESY spectrum of a 10 mM solution of Red. No cross peaks are observed, which is likely due to the strong peak broadening of signals b and c.
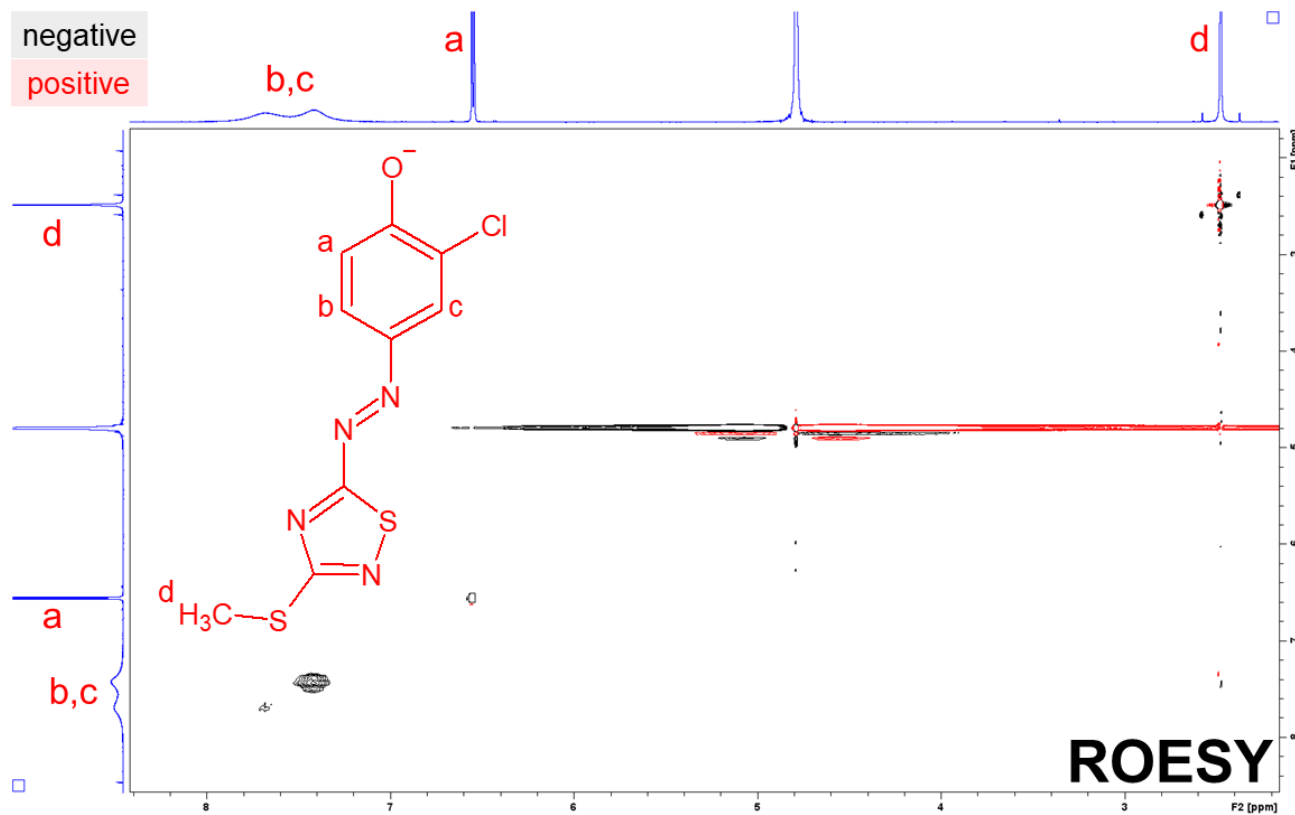
Figure SI15: ROESY spectrum of a solution containing $[Red]_{tot}$ = 10 mM in an $NaHCO_3/Na_2CO_3$ buffer (pD = 10.7, $I \approx 0.25$ M) prepared in D_2O. Negative peaks are shown in black, whereas peaks with positive intensities are shown in red.

Source Code: Determination of Blue dimer spectrum (Python 3)

```
import numpy as np
from scipy.optimize import leastsq

#conc = 1-dimensional array containing concentrations of Blue
#A_exp = 1-dimensional array with length of conc,
#       contains experimental values of absorbance at respective concentration
#spectra = 2-dimensional array with number of lines corresponding to number of
#          wavelengths and number of colums corresponding to number of concentrations,
#          contains experimental data
#p = array containing initial guess of parameters
#K_in = initial guess of dimerization constant
#e_list = array containing initial guess of dimer spectrum
#       (spectrum of sample with highest concentration of Blue used)
#wavelengthlist = array containing wavelengths

p = np.concatenate((K_in,e_list))

def A_red_theo(conc,e_M,KD,e_D):
    A_red = np.zeros(len(conc))
    for i,ctot in enumerate(conc):
        A_red[i] = (e_D*(ctot/2-(np.sqrt(1+8*KD*ctot) - 1)/(8*KD))+e_M*(np.sqrt(1+8*KD*ctot)-1)/(4*KD))
    return A_red

def err_loc(conc,A_exp,e_M,KD,e_D):
    return np.subtract(A_exp,A_red_theo(conc,e_M,KD,e_D))

def err_glob(p,conc,spectra):
    errors = np.zeros([0])
    KD = p[0]
    for i,l in enumerate(wavelengthlist):
        e_M = monomer_E[i] #molar extinction coefficient of monomer at given wavelength
        A_exp = spectra[i]
        e_D = p[i+1]
        errors = np.concatenate((errors, err_loc(conc,A_exp,e_M,KD,e_D)))
return(errors)

popt, pcov, infodict, errmsg, success = leastsq(err_glob,p,args = (conc, spectra),full_output=1)
residuals = err_glob(popt,conc,spectra)
squaredresiduals = np.square(residuals)
chisqu = np.sum(squaredresiduals)
redchisqu = chisqu/(len(residuals)-len(p))
KD = popt[0]
errKD = np.sqrt(pcov[0][0]*redchisqu)
dimerspectrum = np.zeros([len(wavelengthlist),3])
for i,(par,dev) in enumerate(zip(popt,np.diagonal(pcov))):
    if i == 0:
        pass
    else:
        dimerspectrum[i-1,0] = wavelengthlist[i-1]
        dimerspectrum[i-1,1] = par
        dimerspectrum[i-1,2] = np.sqrt(dev*redchisqu)
        pass
```

REFERENCES.

1   W. Schärtl, *Light Scattering from Polymer Solutions and Nanoparticle Dispersions*, Springer Berlin Heidelberg, Berlin, Heidelberg, 2007.

2   Mantid Project, Mantid (2013): Manipulation and Analysis Toolkit for Instrument Data http://dx.doi.org/10.5286/SOFTWARE/MANTID.

3   O. Arnold, J. C. Bilheux, J. M. Borreguero, A. Buts, S. I. Campbell, L. Chapon, M. Doucet, N. Draper, R. Ferraz Leal, M. A. Gigg, V. E. Lynch, A. Markvardsen, D. J. Mikkelson, R. L. Mikkelson, R. Miller, K. Palmen, P. Parker, G. Passos, T. G. Perring, P. F. Peterson, S. Ren, M. A. Reuter, A. T. Savici, J. W. Taylor, R. J. Taylor, R. Tolchenov, W. Zhou and J. Zikovsky, *Nuclear Instruments and Methods in Physics Research Section A: Accelerators, Spectrometers, Detectors and Associated Equipment*, 2014, **764**, 156–166.

4   P. Lindner and T. Zemb, Eds., *Neutrons, X-rays, and light: scattering methods applied to soft condensed matter*, Elsevier, Amsterdam ; Boston, 1st ed., 2002.

5   H. E. Gottlieb, V. Kotlyar and A. Nudelman, *J. Org. Chem.*, 1997, **62**, 7512–7515.

6   M. Kasha, *Radiation Research*, 1963, **20**, 55–70.

7   F. Cuétara-Guadarrama, M. Vonlanthen, K. Sorroza-Martínez, I. González-Méndez and E. Rivera, *Dyes and Pigments*, 2021, **194**, 109551.

8   A. R. Monahan and D. F. Blossey, *J. Phys. Chem.*, 1970, **74**, 4014–4021.

9   E. G. McRae and M. Kasha, in *Physical Processes in Radiation Biology*, eds. L. Augenstein, R. Mason and B. Rosenberg, Academic Press, 1964, pp. 23–42.

10 M. Kasha, H. R. Rawls and M. A. El-Bayoumi, *Pure and Applied Chemistry*, 1965, **11**, 371–392.

11 K. K. Rohatgi, *Journal of Molecular Spectroscopy*, 1968, **27**, 545–548.

12 B. Neumann, K. Huber and P. Pollmann, *Phys. Chem. Chem. Phys.*, 2000, **2**, 3687–3695.

13 A. Belay, *Food Chemistry*, 2010, **121**, 585–590.

14 P. W. Atkins and J. De Paula, *Atkins' Physical chemistry*, Oxford University Press, Oxford ; New York, 10th edn., 2014.

15 E. F. McCoy and I. G. Ross, *Aust. J. Chem.*, 1962, **15**, 573–590.

16 G. J. T. Tiddy, D. L. Mateer, A. P. Ormerod, W. J. Harrison and D. J. Edwards, *Langmuir*, 1995, **11**, 390–393.

17 I. Livsey, *J. Chem. Soc., Faraday Trans. 2*, 1987, **83**, 1445–1452.

18 Schrödinger LCC, PyMOL Molecular Graphics System, Version 1.2r3pre https://pymol.org/2/.

19 J. Teixeira, *J Appl Cryst*, 1988, **21**, 781–785.

20 P. Denkinger and W. Burchard, *Journal of Polymer Science Part B: Polymer Physics*, 1991, **29**, 589–600.

21 K. Huber, W. Burchard, S. Bantle and L. J. Fetters, *Polymer*, 1987, **28**, 1997–2003.

22 K. Huber and W. Burchard, *Macromolecules*, 1989, **22**, 3332–3336.

23 K. Huber, W. Burchard, S. Bantle and L. J. Fetters, *Polymer*, 1987, **28**, 1990–1996.